Biomaterials Advances 182 (2026) 214692

Contents lists available at ScienceDirect

Biomaterials Advances

journal homepage: www.journals.elsevier.com/materials-science-and-engineering-c

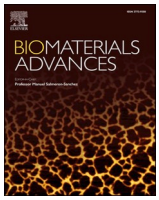

Cellular uptake of anisotropic microparticles in 2D and 3D culture systems

Navneet Kaur [a,b], Annie Scutte [a,b], Mary Jean Savitsky [a,b], Qi Wang [a,b], Pitchaimari Gnanasekar [a,b], Hannah Matos Pimentel [a,b], Dazhi Yang [c], Jamel Ali [a,b,*]

[a] Department of Chemical and Biomedical Engineering, FAMU-FSU College of Engineering, Tallahassee, Florida, 32310, USA
[b] National High Magnetic Field Laboratory, Tallahassee, Florida, 32310, USA
[c] Acrogenic Technologies Inc., Rockville, MD, 20850, USA

ARTICLE INFO

Keywords:
Cellular uptake
3D cell culture
Anisotropic microparticles
Tissue engineering
Confocal microscopy

ABSTRACT

Three-dimensional (3D) cell culture models offer a more physiologically relevant alternative to traditional two-dimensional (2D) cultures by better replicating *in vivo* microenvironments, including extracellular matrix interactions, cell-cell contacts, and nutrient gradients. While nanoparticle uptake in 3D cultures has been extensively characterized, microparticle internalization remains less explored. Here we evaluate cellular uptake of monodisperse anisotropic hematite microparticles of varying geometry (cubic, ellipsoidal, and rod-shaped), synthesized *via* a sol-gel method, in both 2D and 3D cultured normal and cancer cell lines. Using a combination of microscopy and spectroscopy, we reveal shape-dependent uptake patterns, with rod-shaped microparticles exhibiting significantly enhanced internalization, particularly within 3D cancer spheroids. Confocal *Z*-stack imaging further demonstrated deeper penetration of rod-shaped particles into spheroid cores compared to other shapes, underscoring the influence of particle aspect ratio and cellular microenvironment on uptake efficiency. Cytotoxicity assays highlight differential responses in 2D *versus* 3D cultures, emphasizing the importance of 3D models for evaluating therapeutic platforms. These findings advance the understanding of microparticle behavior in complex tissue-like environments, supporting their potential for improved drug delivery, tissue engineering, and regenerative medicine applications.

1. Introduction

Two-dimensional (2D) cell culture is a conventional approach for investigating cellular behavior and responses *in vitro*. A widely accepted method to analyze cell responses to stimuli [1], 2D cell culture involves growing cells on flat surfaces, typically in petri dishes or flasks. This method allows for easy observation and manipulation of cells; however, these conditions do not accurately mimic the natural conditions found *in vivo*, including the complexity of tissue microenvironments and cell-cell interactions, [2]. Thus it is challenging to predict and understand how native tissues will respond to therapies using 2D *in vitro* models. To overcome this shortcoming, the development of 3D cell culture models has emerged as a promising alternative that better recapitulates the complexity and heterogeneity of tissues [3], by providing cells with a more realistic microenvironment, including the presence of extracellular matrix components, cell-cell interactions, and nutrient gradients [4], better insight into cell proliferation, differentiation, migration, and drug sensitivity can be gleaned. Multiple techniques, including hanging-drop, forced-floating, and agitation-based approaches have been used for creating 3D cell culture systems [5–9]. Moreover, investigations with artifical scaffolds, where cells are embedded within a matrix, have increased significantly due to their ability to closely resemble the properties of natural extracellular matrix (ECM) [5,6,10,11]. For example, human tissue-derived extracellular matrix (hDAM) scaffolds have offered a biomimetic 3D microenvironment for breast cancer cell growth and drug testing. Cultures with hDAMs have been demonstreated to accurately recapitulate *in vivo* conditions compared to traditional 2D cultures, showing distinct differences in cell proliferation, migration, morphology, and drug response [12]. Similar matrices have been also used to form 3D tumor models, where cancer cells self-assemble to form multicellular spheroids. Using these materials for 3D culture, drug screening assays have shown increased cellular resistance to anticancer agents than traditional cultures, highlighting their potential for more predictive *in vitro* drug testing [13].

Nanoparticles are promising candidates for a variety of biomedical applications, such as drug delivery and tissue engineering, due to their

* Corresponding author at: Department of Chemical and Biomedical Engineering, FAMU-FSU College of Engineering, Tallahassee, Florida, 32310, USA.
E-mail address: jali@eng.famu.fsu.edu (J. Ali).

https://doi.org/10.1016/j.bioadv.2025.214692
Received 8 August 2025; Received in revised form 22 December 2025; Accepted 26 December 2025
Available online 28 December 2025

distinctive characteristics and functions [14–17]. There have been several reports on nanoparticle uptake in both 2D and 3D cell cultures [18–20]. In recent work, human gut organoids and spheroids (400 μm in size) were used to assess nanoparticle uptake, revealing that both 2D and 3D cultures allow thorough nanoparticle penetration. Doxorubicin-loaded nanoparticles penetrated deeper into tumor spheroids than dissolved drugs, highlighting the potential of *in vitro* intestinal models for developing nanomedicines for localized therapy [19]. Besides nanoparticles, microparticles have attracted significant attention over the past decades due to their unique properties and versatility. Microparticles are defined as particles with diameters ranging from 1 to 1000 μm. Microparticles offer several advantages over nanoparticles. Particles larger than 100 nm generally remain localized without crossing the interstitium *via* lymphatic transport, producing stronger local effects, and show improved retention in the skin. Pulmonary delivery benefits from particles under 10 μm, which reach the alveolar region, while particles below 20 μm can be phagocytosed upon entering the bloodstream. Microparticles can be made into solid, liquid, or semi-solid dose forms that can be administered subcutaneously, intravenously, intramuscularly, or orally. In vaccine formulations, they improve solubility and bioavailability, co-deliver numerous bioactive ingredients, facilitate controlled, prolonged, and targeted release, and boost immune responses. As a result, they play an important role in pharmaceutical and biomedical research, particularly in drug delivery, tissue engineering, regenerative medicine, imaging, biosensing, and diagnostic applications. Their customizable size, composition, and surface functionality enable precise control of biological interactions [21,22].

The shape of microparticles plays a crucial role in their biological activity, especially in the uptake of particles. Particle geometry strongly influences adhesion, endocytosis, circulation, and biodistribution. Spherical particles are often internalized more rapidly, whereas discoidal or elliptical particles show prolonged circulation and improved targeting. Cylindrical or rod-shaped microparticles can trigger enhanced cellular uptake and stronger biological responses compared with spheres, with aspect ratio further dictating uptake efficiency. Beyond overall geometry, the local curvature and orientation of a particle at the cell–membrane interface also determine whether phagocytosis occurs, as regions of high curvature favor internalization. These findings demonstrate that both global and local shape features critically affect particle–cell interactions, drug influx, and therapeutic efficiency [23,24]. Such insights highlight the growing importance of shape-engineered microparticles in drug delivery, tissue engineering, and mechanobiology, and provide the foundation for our study, which investigates the effects of diverse microparticle geometries in 2D and 3D culture systems [25,26].. Moreover, physical properties of 3D matrix also affect the uptake of nano/microparticles by cells. It is reported that with the increase in network stiffness and density, there is a decrease in the ability of nano/microparticles diffusion [27]. Moreover, in 3D matrices, cellular uptake mechanisms include complex processes that are significantly distinct from those observed in 2D cultures owing to the distinct environments, cells exhibit altered phenotypes, including distinct morphology, altered gene expression profiles, and modified cell signaling pathways [28–30]. These factors can significantly impact particle internalization kinetics and intracellular trafficking routes. However, despite a large body of work on nanoparticles, there are much fewer reports on the uptake of microparticles, especially with respect to non-spherical microparticles, in 2D and 3D cultures.

Understanding the interactions of microparticles with 2D and 3D cultured cells can lead to the discovery of novel strategies to enhance the effectiveness of microparticle-based drug delivery systems. One key aspect of microparticles-cell behavior is the role of shape-dependent interaction, where the larger size and varied geometries of these microparticles facilitate investigation *via* microscopy. Here we investigate the impact of geometry and cell type toward evaluating the role of shape in microparticle drug delivery platforms. Differences in the uptake of anisotropic microparticles, such as their unique physical properties and varied interactions with normal and cancer cell lines, are assessed.

2. Results and discussion

Hematite (Fe_2O_3) microparticles of similar size but varying geometry were synthesized through a sol-gel approach (Fig. 1A) and displayed. Analysis of micrographs of synthesized particles taken with scanning electron microscopy (SEM) revealed that the microparticles synthesized without Na_2SO_4 exhibited a pseudo-cubic morphology with size ~1.2 μm, while those synthesized with Na_2SO_4 displayed ellipsoid (~1.3 μm long, 0.9 μm wide), and rod-shaped structures (~1.6 long, 0.5 μm wide), indicating a change in the crystallization process due to the presence of Na_2SO_4 (Fig. 1B). This control over particle morphology is due to Na_2SO_4 influencing the ionic environment, thereby affecting the nucleation and growth processes, which promotes anisotropic particle formation. X-ray diffraction (XRD) spectra of all the synthesized hematite nanostructures appeared similar, regardless of their shapes (cubic, ellipsoid, or rod). The diffraction peaks, as shown in Fig. 1C, corresponded to the rhombohedral phase of α-Fe_2O_3, specifically from the (104), (110), (113), (024), (116), and (300) crystallographic planes. This confirmed that the resulting iron oxide nanostructures were consistent with the crystalline hematite (α-Fe_2O_3) phase, with lattice constants of $a = 5.037$ Å and $c = 13.75$ Å, as reported by Jiang et al [31]. The sharp and well-defined XRD peaks further indicated that the nanostructures were highly crystalline and corresponded to the pure rhombohedral phase of α-Fe_2O_3. Additionally, no impurity peaks were observed, suggesting that the particles were largely free of other elements. An Energy Dispersive X-ray (EDX) analysis validated the elemental composition, showing the presence of iron (Fe) and oxygen (O) uniformly distributed across the particles. The EDX analysis revealed in Fig. 1D showed that these microparticles were composed of ~30 % oxygen and ~ 70 % iron by weight. The EDX spectrum showed only peaks corresponding to Fe and O atoms, indicating that no impurities were present during the synthesis of the material.

NIH3T3 fibroblasts and MDA-MB-231 breast cancer cells were cultured with a micro-fibrous biomaterial to assess spheroid formation and growth over time. Bright-field microscopy analysis revealed that spheroids began forming around day 3 for both cell types. Over time, the spheroids continued to grow, showing a steady increase in diameter by day 28 (Fig. 2).

spheroids were slightly smaller at 332 μm (Fig. S1). This difference in size might be because the two cell types grow differently in the microfibrous material. The observed increase in spheroid size over time reflects successful cellular proliferation and aggregation within the microfibrous environment. This progressive growth trend supports the potential of the biomaterial scaffold for long-term cell culture, making it a promising model for studying cell behavior in 3D models. Scanning electron microscopy imaging of the scaffold (Fig. 2C) revealed a well-organized, porous structure with an interconnected network of fibers and pores. This fibrous network mimics the *in vivo* microenvironment for the growth and development of cells. Interaction between matrix and the cells was shown in Fig. 2D, demonstrating that cells adhered to the matrix with strong cell-matrix interactions that are essential for promoting cell survival, proliferation, and migration in a 3D environment. Cell viability assays were conducted on both NIH3T3 (Fig. 2E) and MDA-MB-231 (Fig. 2F) cells cultured in the 3D matrix showed high survival rates for both cell types. Results demonstrated high survival rates for both cell types, suggesting that the matrix provides a supportive environment that promotes cell viability. The cell viability was measured using a MTT assay, with absorbance readings taken at 545 nm. The data showed a progressive increase in absorbance over time, indicating that cell viability and proliferation were increasing with each successive day. This suggests that the 3D matrix supports not only cell survival but also cellular proliferation over time, an essential factor for applications in tissue engineering and 3D cell culture studies.

After culturing spheroids of NIH3T3 and MDA-MB-231 for 7 days, we

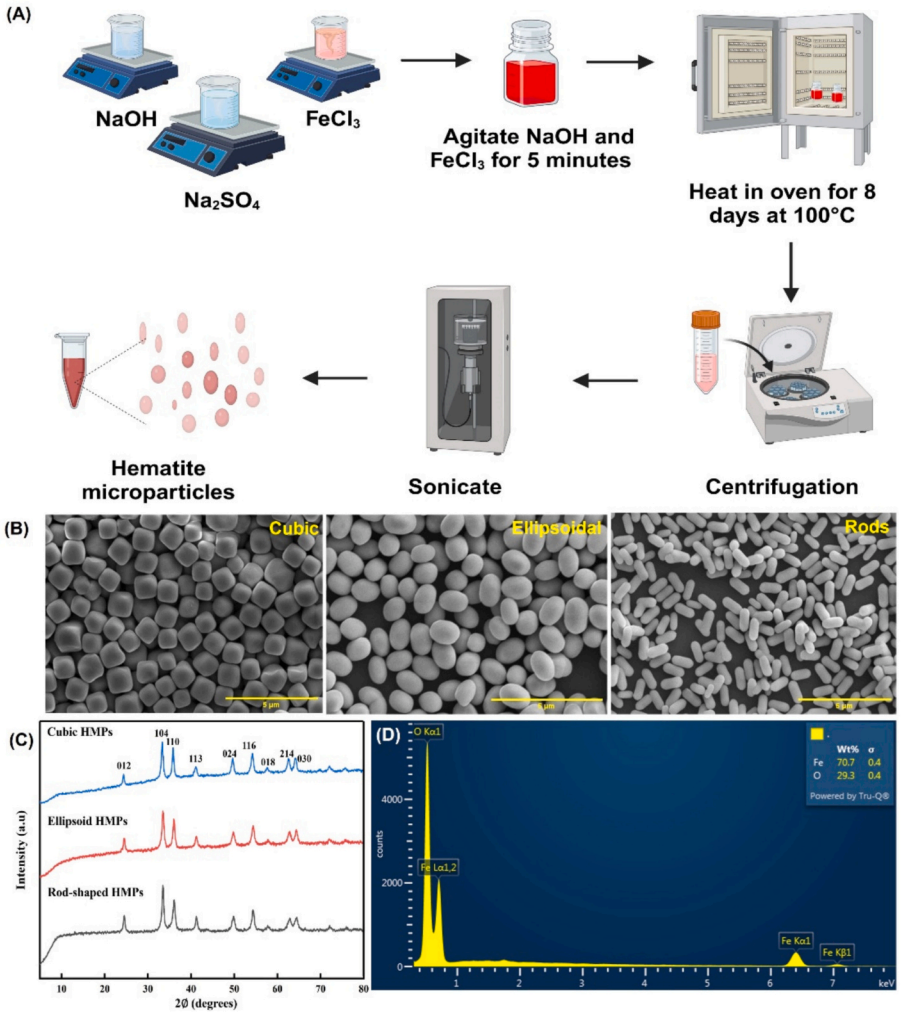

Fig. 1. (A) Schematic representation of synthesis of different shaped hematite microparticles, SEM images of microparticles (B) Cubic, ellipsoidal, rod shaped, (C) XRD spectra of synthesized hematite particles, and (D) EDX spectra with elements percentages.

treated them with hematite microparticles of various geometry, cubic, ellipsoidal, and rod-shaped, for 24, 48, and 72 h. The uptake of these particles was monitored over time using brightfield imaging (Fig. 3). It was observed that particle uptake increased with longer exposure time. At 24 h, most of the particles were seen outside of spheroids, while by 72 h, there was a noticeable increase in particle internalization, as indicated by the enhanced contrast in the brightfield images for both cell types. Upon comparing the geometry of the microparticles, rod-shaped particles exhibited the highest contrast within the spheroids, suggesting significantly greater uptake than ellipsoidal and cubic particles in both NIH3T3 (Fig. 3A) and MDA-MB-231 (Fig. 3B).

We captured reflective brightfield images (insets at 48 h), which enhanced the visualization of microparticles due to their reflective properties, allowing for clearer observation of particle distribution within and around the cell clusters. In the reflective images, the microparticles appeared brighter against the background, making it easier to distinguish their locations. This imaging mode confirmed that rod-shaped and ellipsoidal particles show higher uptake as evidenced by their increased brightness within the cell clusters. The difference in uptake can be attributed to the aspect ratio, which plays a crucial role in cellular internalization. The aspect ratio, defined as the ratio of length to width, affects how particles interact with the cell membrane and penetrate cellular structures. Rod-shaped particles have a higher aspect ratio compared to cubic and ellipsoidal particles, which may enhance their ability to align with and penetrate the cell membrane, leading to increased membrane wrapping and endocytosis [32]. In contrast, cubic particles have a lower aspect ratio, resulting in a reduced surface area in contact with the cell membrane, which may limit their uptake. Their shape could also cause steric hindrance during internalization, making it more challenging for cells to engulf them. Ellipsoidal particles, with an intermediate aspect ratio, showed moderate uptake, falling between rod-shaped and cubic particles in terms of internalization efficiency. These results highlight the importance of particle geometry in influencing cellular uptake of microparticles within 3D cell cultures. Similar results were observed in 2D cell cultures, where rod-shaped particles also demonstrated superior uptake over cubic and ellipsoidal shapes (Fig. S2). This consistency suggests that the higher aspect ratio of rod-shaped particles improves cellular uptake across both 2D and 3D models.

To further validate the microparticle uptake results, we performed confocal imaging for live/dead staining along with the control group. The live/dead images confirmed that cells remained predominantly viable following exposure to cubic, elliptical, and rod-shaped microparticles, indicating that the observed particle internalization was not a consequence of cytotoxic effects. The control group without microparticles showed normal morphology and viability, supporting that the staining and imaging conditions did not induce background artifacts (Fig. 3 (C) and (D).

Furthermore, the uptake of microparticles by 3D-cultured spheroids from NIH3T3 and MDA-MB-231 cells was examined using SEM with two

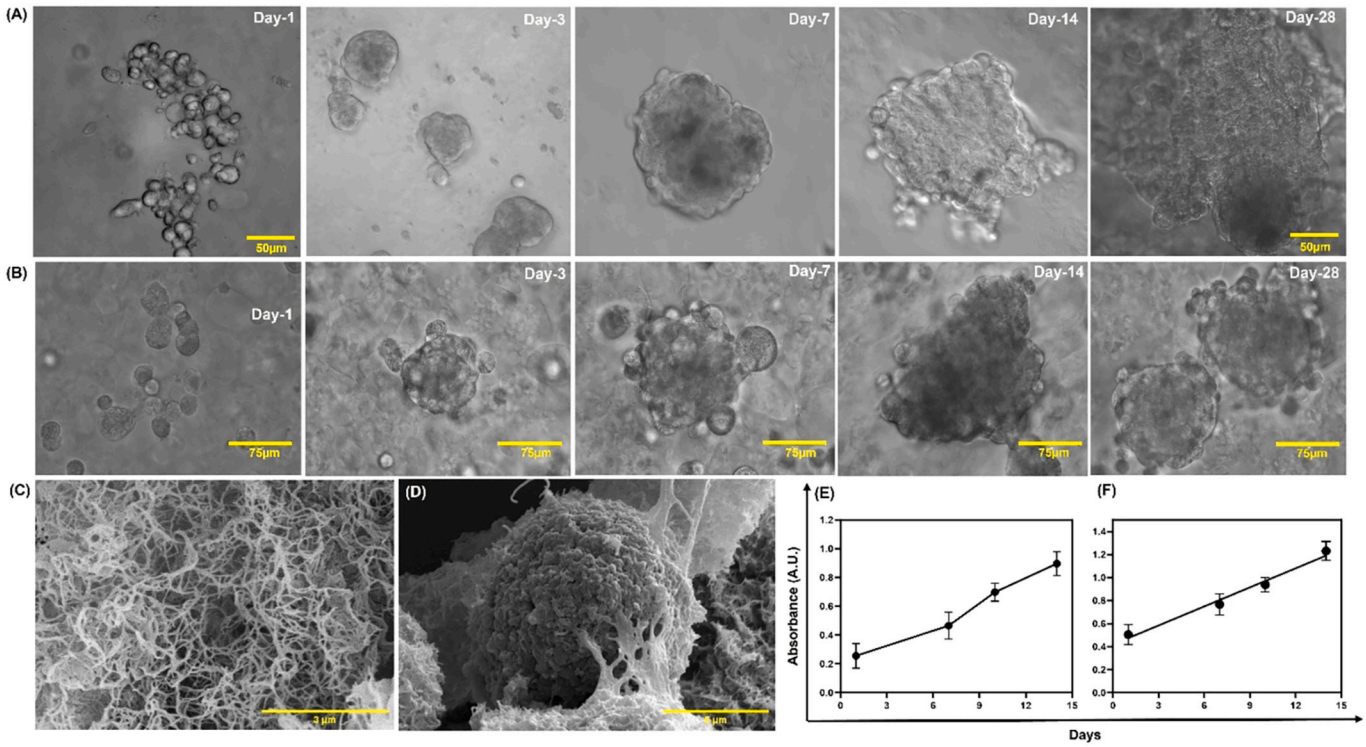

Fig. 2. Brightfield images of 3D cultured (A) NIH3T3 and (B) MDA-MB-231 for 28 days, SEM images of (C) micro-fibrous biomaterial, (D) Interaction of scaffold with cells, cell viability of cultured (E) NIH3T3 and (F) MDA-MB-231 spheroids within micro-fibrous scaffold.

detectors: the Everhart-Thornley Detector (ETD) and the Concentric Backscattered Detector (CBS). The ETD is typically used to capture low-energy secondary electrons, providing detailed topographical information of the sample surface. In this work, images obtained with the ETD revealed the presence of microparticles on the outer surface of both NIH3T3 and MDA-MB-231 cell spheroids. However, the ETD did not provide sufficient information regarding the internal localization of these particles within the 3D structures. In contrast, the CBS detector is designed to capture internal details by utilizing backscattered electrons, which are more sensitive to compositional differences within the sample. The backscattered electrons are generated through elastic collisions with atomic nuclei, revealing internal structures and material composition [33,34]. Using the CBS detector, we observed significant internalization of microparticles within the spheroids. The CBS images clearly show that the microparticles were not only attached to the surface but penetrated deeper into the 3D-cultured spheroids (Fig. 4). Moreover, the uptake of particles was higher in MDA-MB-231 spheroids compared to NIH3T3 spheroids, indicating a potential difference in cellular uptake mechanisms between these two cell types and cancerous MDA-MB-231 cells may facilitate enhanced uptake, due to altered cellular processes or differences in spheroid structure compared to the NIH3T3 cells. Furthermore, rod-shaped particles exhibited higher internalization in both cell types as shown by CBS images in comparison to cubic particles. These results suggest that rod-shaped and ellipsoidal particles are more readily internalized by 3D spheroid models, especially in cancer-derived MDA-MB-231 cells. Moreover, we did SEM analysis for the uptake of microparticles in 2D cultured NIH3T3 and MDA-MB-231 cells where rod-shaped and ellipsoidal microparticles showed higher uptake in both cell lies as compared to cubic microparticles (Fig. S3). Furthermore, EDX imaging confirmed the presence of iron (Fe) and oxygen (O) within the cells, indicating the uptake of hematite microparticles (Fe_2O_3) (Fig. S4).

Moreover, we employed focused ion beam (FIB) to further confirm the presence and distribution of the microparticles within the spheroids. MDA-MB-231 spheroids treated with microparticles were fixed and coated with conductive material to prevent charging during imaging. The FIB technique utilizes a focused ion beam to cut thin sections of the spheroid, enabling the visualization of both surface and internal structures at high resolution. The SEM captured detailed images of the spheroid's surface, while the ion beam sectioned through the spheroid, revealing cross-sections, and offering a 3D view of the internal cellular structure. The microparticles, appearing as bright objects due to their high contrast with the surrounding cellular material, were observed within the spheroids (Fig. 5). The SEM images also showed the localization of the microparticles, revealing whether they were confined deeper into the inner cell layers of spheroids. Also, it highlighted the interaction between the microparticles and the extracellular matrix. Thus, it showed the microparticles are internalized by spheroids.

Further, we treated both 2D and 3D cultured cells with all three types of microparticles at varying concentrations (12.5, 50, 100, 200, and 400 μg/mL) and assessed their toxicity using an MTT assay. The results showed that 2D cultured cells were more sensitive to the microparticles compared to 3D cultured cells. As the concentration of microparticles increased, toxicity also increased in both 2D and 3D cultures. At concentrations of 400 μg/mL, the microparticles exhibited significant toxicity in both culture types (Fig. S5). Moreover, both 2D and 3D cultured cancer cells were more affected by the microparticles than normal cells, indicating that the cancer cells are more susceptible to the toxicity of the microparticles than normal fibroblast cells.

To further confirm the uptake of microparticles, we also performed confocal microscopy. Confocal *Z*-stack images of MDA-MB-231 and NIH3T3 spheroids (Fig. 6, panels A and B) reveal distinct differences in microparticle uptake based on both cell type and spheroid morphology. The Z-stack series, presented with increasing imaging depth from left to right, enables visualization of microparticle distribution from the spheroid core toward the outer layer. In these images, cell nuclei were stained using DAPI (blue) and TRITC (red), allowing clear visualization of cellular organization and spheroid architecture. Microparticles were visualized using reflectance imaging *via* a Nikon AX confocal system, captured in the green channel, providing strong contrast against the

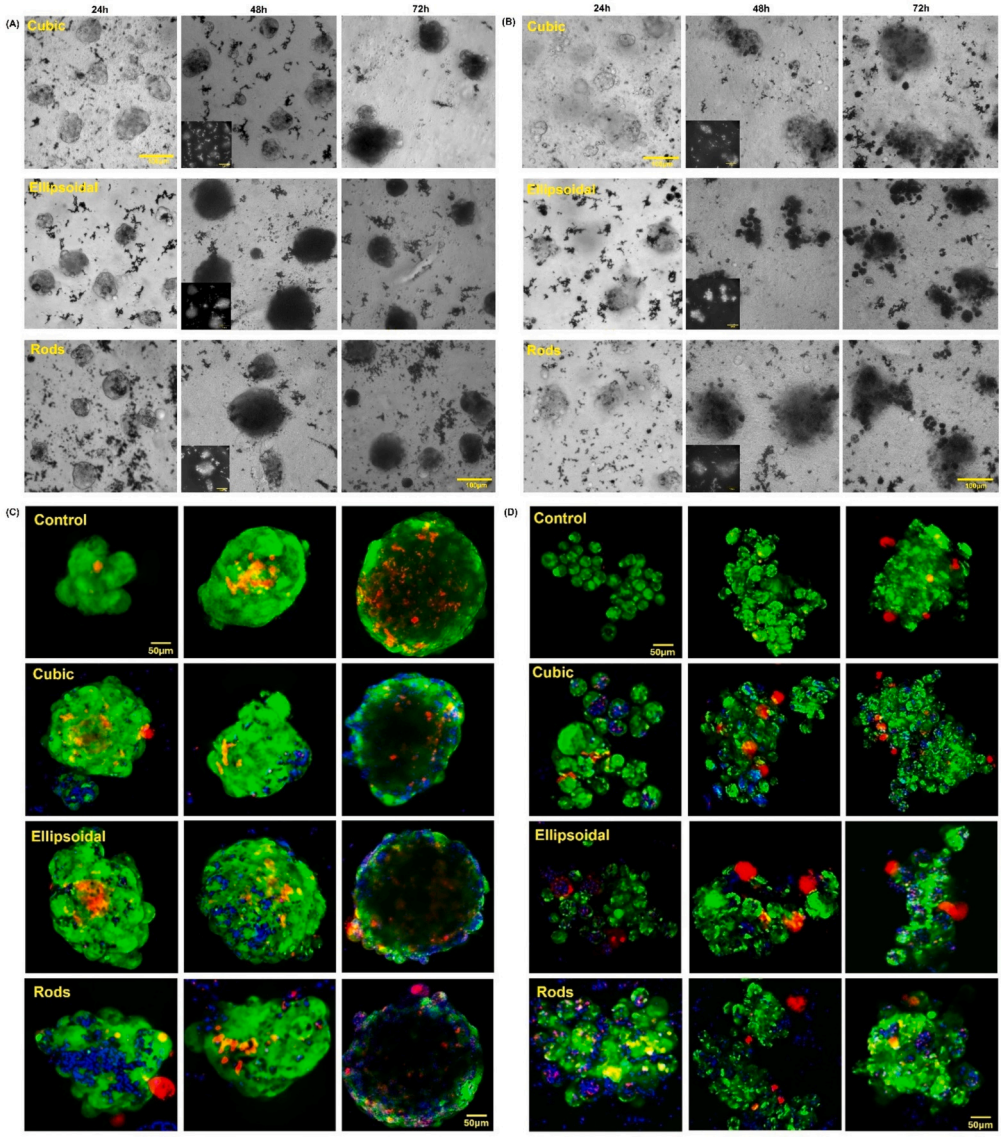

Fig. 3. Brightfield images of 3D cultured (A) NIH3T3 cells and (B) MDA-MB-231 cells after treatment with microparticles, cubic, ellipsoidal, and rod-shaped for 24, 48, 72 h. Insets show reflection images of spheroids containing microparticles. Confocal live/dead imaging of (A) NIH3T3 spheroids and (B) MDA-MB-231 spheroids showing live/dead staining of cells interacting with particles of varying geometries; cubic, ellipsoidal, and rod-shaped. Viable cells appear green, dead cells appear red, and particles appear blue due to their intrinsic reflectance signal. (For interpretation of the references to colour in this figure legend, the reader is referred to the web version of this article.)

other stains [35]. Reflectance confocal microscopy was employed in this study to visualize the distribution of microparticles within the 3D spheroids. Unlike fluorescence imaging, reflectance microscopy detects light reflected from the surface of materials with high refractive indices such as iron oxide allowing clear visualization of unlabeled metallic or inorganic particles without the need for additional staining or surface modification. This technique provides non-invasive, label-free imaging and preserves the physicochemical integrity of the microparticles [35,36].

In MDA-MB-231 spheroids, particularly those with rod-shaped morphology, microparticles are observed penetrating more deeply and in greater numbers compared to the cubic and ellipsoidal morphologies. In contrast, NIH3T3 spheroids show overall lower uptake, with most particles remaining near the periphery, regardless of morphology. High-magnification, confocal-focused images (panels C and D) further confirm the internalization of microparticles (Fig. S6). Rod-shaped MDA-MB-231 spheroids show strong internal reflectance signals in the green channel, suggesting effective microparticle penetration and internalization throughout the spheroid.

This difference can be attributed to the highly invasive and metabolically active nature of MDA-MB-231 breast cancer cells, which exhibit enhanced membrane fluidity and elevated endocytic activity, thereby promoting more efficient microparticle uptake. In contrast, NIH3T3 spheroids, derived from normal fibroblasts, possess a more compact structure and lower metabolic rate, resulting in reduced cellular uptake. The weaker and more localized reflectance signals observed in NIH3T3 spheroids therefore suggest that the microparticles largely remain near the spheroid periphery, indicating limited internalization compared to the more permeable and dynamic MDA-MB-231 spheroids [37–39].

Quantitative analysis of particle uptake (Fig. 6, panel E) supports the qualitative observations from the confocal images. Both cell lines display the lowest percentage uptake in cubic and ellipsoidal spheroids. In MDA-MB-231 rod-shaped spheroids, however, microparticle uptake increases dramatically approximately threefold compared to the other morphologies, highlighting a strong correlation between shape and

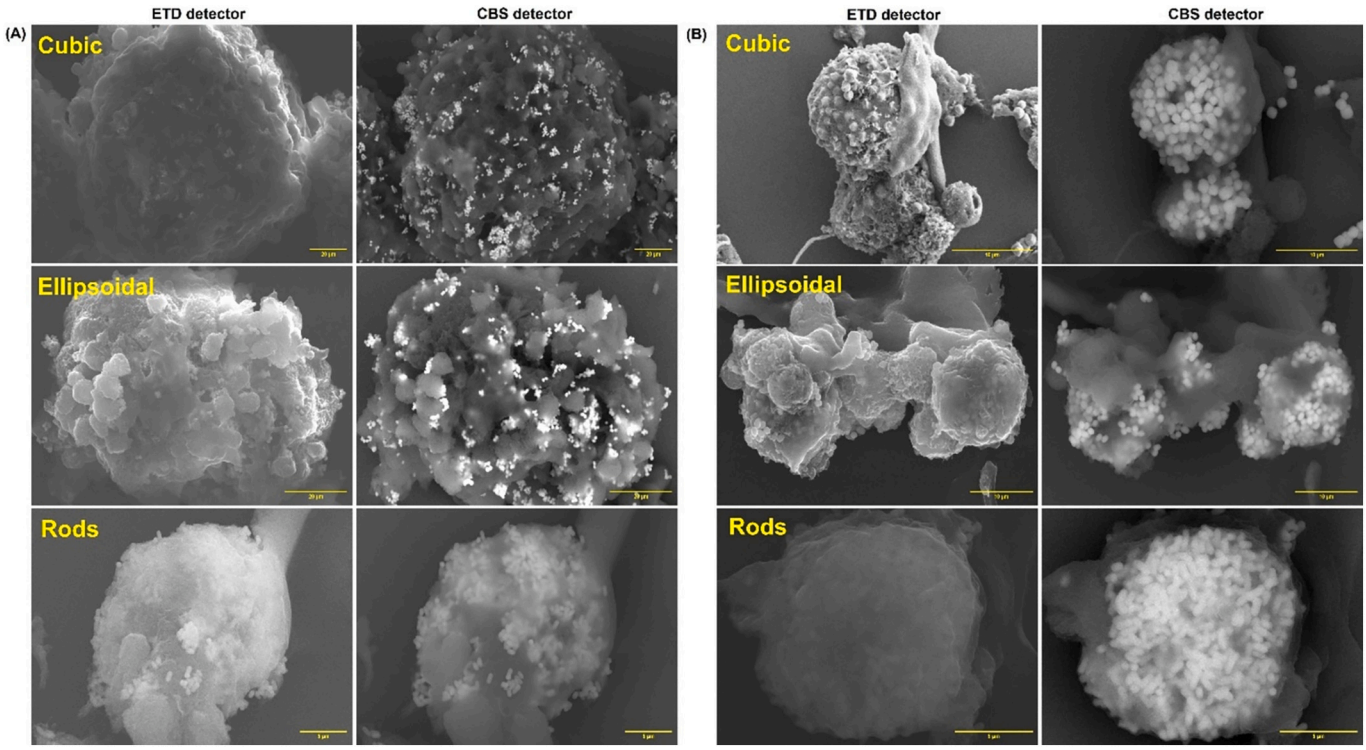

Fig. 4. SEM with two different detectors, ETD and CBS, show uptake of microparticles: cubic, ellipsoidal, rod-shaped by 3D-cultured (A) NIH3T3 cells and (B) MDA-MB-231 cells after treatment.

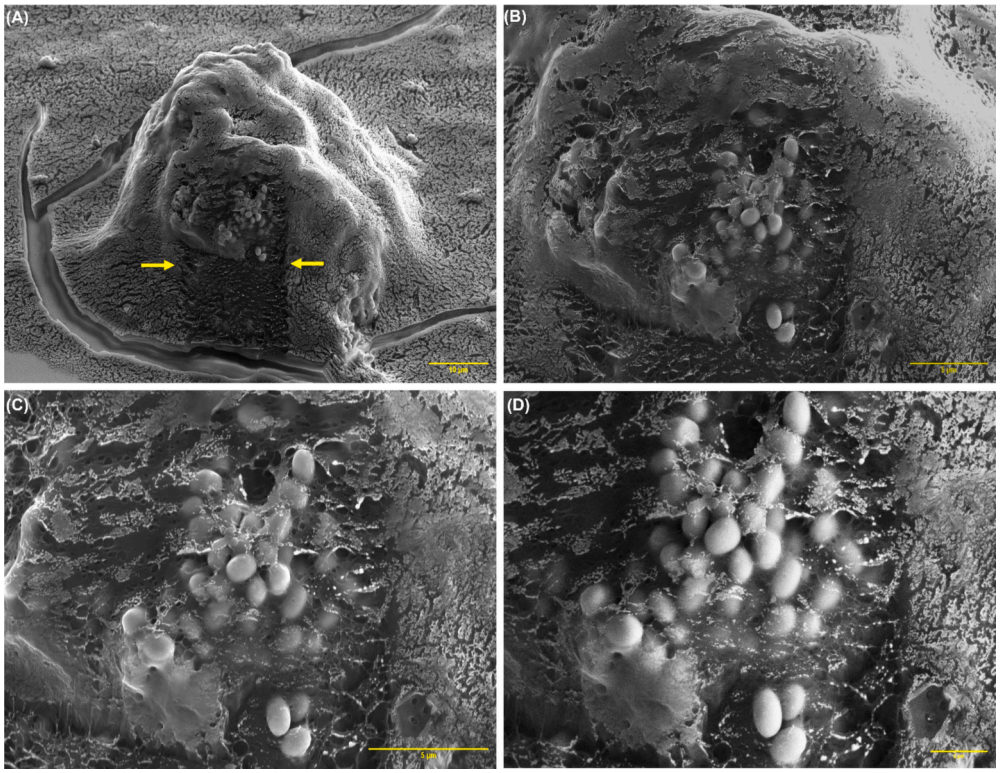

Fig. 5. Focused ion beam scanning electron microscopy images of MDA-MB-231 spheroids treated with microparticles, showing uptake of microparticles. Yellow arrows indicate the FIB cut site used for cross-sectional imaging. (For interpretation of the references to colour in this figure legend, the reader is referred to the web version of this article.)

uptake efficiency. Rod-shaped NIH3T3 spheroids also showed an increase in uptake relative to their cubic and ellipsoidal counterparts, but the overall levels remain significantly lower than in MDA-MB-231 rod spheroids.

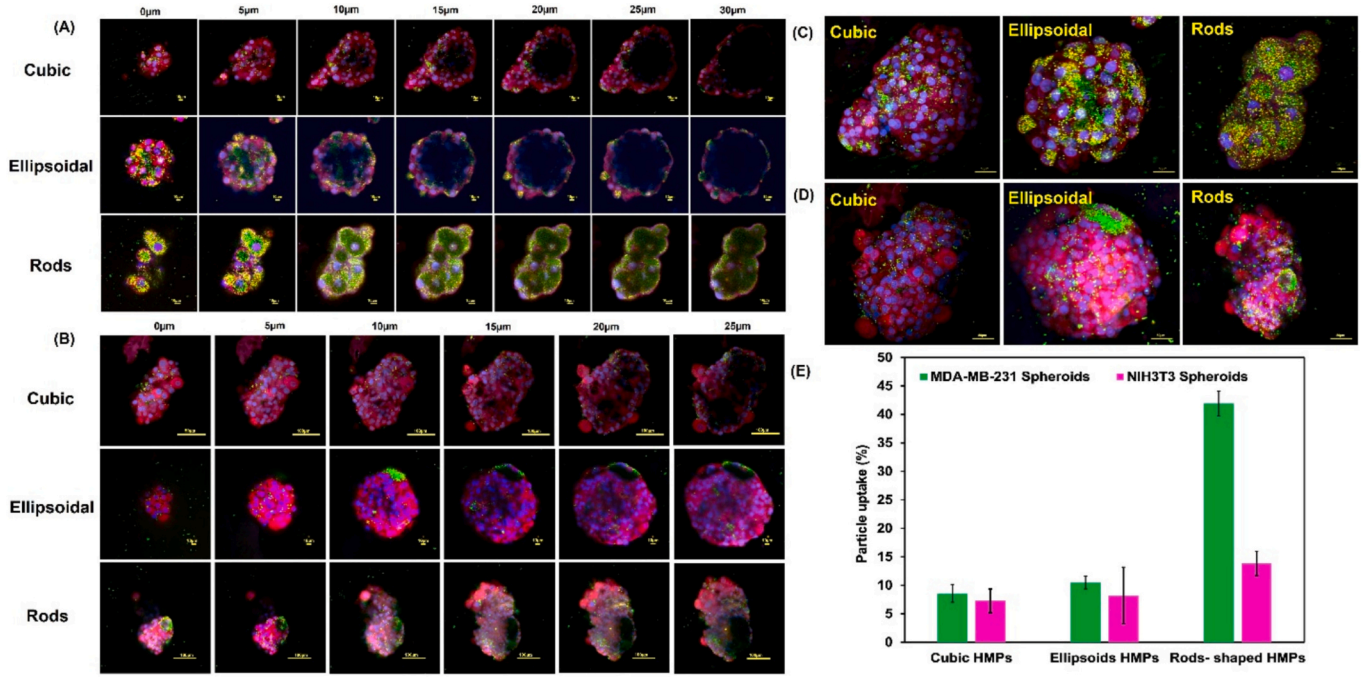

Fig. 6. Confocal microscopy *Z*-stack images showing microparticle uptake in 3D spheroids of (A) MDA-MB-231 and (B) NIH3T3 cells, with increasing imaging depth (height) from left to right, of (C) MDA-MB-231 spheroids and (D) NIH3T3 spheroids showing internalized microparticles (green) with nuclei-stained blue and cytoskeleton-stained red. Each spheroid type includes three morphological categories: Cubic, Ellipsoidal, and Rod-shaped and (E) Quantification of microparticle uptake, presented as the percentage of particle internalization across different spheroid morphologies and cell lines. Data represent mean ± SD (n = X), highlighting morphology- and cell-type-dependent differences in microparticle uptake. (For interpretation of the references to colour in this figure legend, the reader is referred to the web version of this article.)

The enhanced uptake observed in rod-shaped spheroids can be attributed in part to their higher aspect ratio, the ratio of length to width which may facilitate improved microparticle access and interaction with the spheroid surface. A higher aspect ratio can lead to a larger exposed surface area and altered curvature, which may reduce diffusion barriers and enhance permeability [40,41]. Additionally, rod-shaped structures may induce mechanical or biological changes in the cell-cell or cell-matrix organization, creating pathways that promote deeper particle penetration [41]. This geometric influence, coupled with the inherently higher endocytic activity of MDA-MB-231 cells, likely accounts for the significant uptake observed in these rod-shaped cancer spheroids.

Notably, these results are consistent with our previous observations from scanning electron microscopy and optical microscopy, further validating the enhanced uptake behavior in rod-shaped MDA-MB-231 spheroids. Together, these findings underscore the importance of spheroid geometry, particularly aspect ratio and cell type in optimizing microparticle delivery for therapeutic applications.

3. Conclusion

In this investigation, we demonstrated that anisotropic hematite (Fe_2O_3) microparticles exhibit distinct shape-dependent uptake behaviors in both 2D and 3D cultures of fibroblast and epithelial cell lines. Rod-shaped particles showed the highest level of internalization, followed by ellipsoidal and cubic geometries. Confocal *Z*-stack imaging revealed deeper penetration and more extensive uptake of rod-shaped particles, particularly in metabolically active MDA-MB-231 cancer spheroids, whereas in NIH3T3 fibroblast spheroids, particles were primarily localized near the periphery. SEM and EDX analyses corroborated these observations, confirming successful microparticle internalization and relatively higher uptake in cancer spheroids compared to normal ones.

While the analyses in this work were primarily qualitative, imaging-based methods provided reliable visualization of particle–cell interactions without altering the physicochemical properties of the particles. Semi-quantitative reflective imaging (Fig. 6e) enabled comparison of internalization trends across different particle geometries, though it remains shape dependent. Future studies incorporating quantitative approaches, such as flow cytometry with fluorescently labeled or traceable particles, will further elucidate the extent and mechanisms of microparticle uptake in 3D systems.

Overall, our findings underscore the critical influence of particle geometry and 3D cellular architecture on particle internalization and cytotoxic response. The ability of rod-shaped hematite microparticles to achieve enhanced penetration and retention within 3D cancer spheroids highlights their potential as shape-optimized platforms for targeted delivery and tissue engineering applications.

4. Experimental section

4.1. Materials

Iron (III) chloride hexahydride, sodium hydroxide, sodium sulfate, MTT, cytochalasin D, genistein, and chlorpromazine hydrochloride was obtained from Sigma Aldrich (USA). Dulbecco's modified Eagle's medium (DMEM) was purchased from Gen Clone. Penicillin Streptomycin solution and trypsin was obtained from corning, USA.

4.2. Synthesis of hematite microparticles

Hematite microparticles were synthesized with sol-gel method as previously reported [42]. The shape of the particles was controlled by the addition of sodium sulfate. For pseudo cubic microparticles synthesis, 5.4 M NaOH was slowly added to the 2 M $FeCl_3$ solution on stirring. Further, the solution was shaken vigorously to homogenize the gel. The gel was aged in oven at 100 °C for 8 days. After 8 days, particles were centrifuged at 3000 rpm for 10 min and washed with water trice to remove unwanted salt from the particles. 0.2 M and 0.6 M Na_2SO_4 was

added to the homogenized gel before keeping in the oven for ellipsoidal and rod-shaped hematite microparticles respectively.

4.3. Characterization of hematite microparticles

The synthesized particles were investigated using a focused ion beam scanning electron microscopy (FIB-SEM) Helios dual beam G4 UC Thermo Fisher for the size and shape of the particles. The elemental composition was determined by an EDX detector (Oxford Instruments) coupled with the SEM. Crystal phases of hematite particles were confirmed by X-ray diffraction (XRD) (Bruker AXS D2 phaser, Germany).

4.4. 2D Cell culture

Invitro cell studies were carried out with mouse embryonic fibroblasts (NIH3T3) cell line and triple-negative breast cancer (MDA-MB-231) cell line. Both the cell lines were obtained from ATCC and cultured in 75cm^2 and 175cm^2 flasks with DMEM culture medium. Growth medium was supplemented with FBS and antibiotic solution. Cells were maintained in a humified incubator with 5 % CO_2 at 37 °C.

4.5. 3D cell culture

Biomaterial was obtained from Acrogenic Company (Patent No. US-2018094080-A1). It was autoclaved and activated before culturing the cells. Poly-L-lysine based biomaterial was gently mixed with both the cell lines (1×10^6 cells/mL) separately and cells were allowed to grow in low attachment 96-well plates for 7 days. After 7 days, cells were treated with hematite microparticles for further analysis.

4.6. Morphological analysis and cell viability of 3D cultures

Cells were seeded in a scaffold and incubated under standard conditions. For morphological analysis, cultures were examined using a bright field microscope. Images were captured at various times to observe changes in cell morphology, structure, and spatial organization. To assess cell viability, the MTT assay was employed. MTT reagent was added to the cultures and incubated according to the manufacturer's instructions. After incubation, the absorbance at 595 nm was measured using a microplate reader, providing an indication of cell viability based on metabolic activity.

4.7. Cytotoxicity of hematite microparticles

4.7.1. In 2D cultures

NIH3T3 and MDA-MB-231 cells were seeded in 96-well plates at a 1×10^4 cells/mL. Cells were treated with different concentrations pseudo cubic, ellipsoidal, and rod-shaped particles (12.5, 25, 50, 100, 200, 400 μg/mL) for 48 h. After specified incubation period, MTT was added to the cells and further incubated for 1 h. After 1 h, formazan crystals were dissolved with the addition of DMSO, and absorbance was determined with plate reader at 595 nm. Cell viability was calculated as follows:

$$\textit{Cell viability}\ (\%) = \frac{OD595\ (sample) - OD\ 595\ (blank)}{OD595\ (control) - OD\ 595\ (blank)}$$

4.7.2. In 3D cultures

After culturing the both the cell lines with biomaterial for 7 days, cells were treated with different concentrations pseudo cubic, ellipsoidal, and rod-shaped particles (12.5, 25, 50, 100, 200, 400 μg/mL) for 48 h. After a specified period, MTT was added and incubated for 1 h, following incubation SDS-HCl was added to the spheroids, which effectively dissolved the crystals within the dense 3D spheroid matrix. Further cultures were incubated in the CO_2 incubator for 1 h. After 1 h, absorbance was measured at 595 nm with plate reader. Cell viability as calculated with above mentioned equations.

4.8. Live/dead viability assessment

NIH3T3 fibroblast and MDA-MB-321 spheroids were treated with each type microparticles for 24, 48, and 72 h, followed by assessment of cell viability using a live/dead staining assay. At each time point, a staining solution containing calcein-AM to label viable cells and ethidium bromide to label membrane-compromised (dead) cells was added to the cultures in PBS. Spheroids were incubated at 37 °C for 30 min in the dark and then transferred to glass-bottom dishes for imaging. Confocal laser scanning microscopy was used to acquire z-stack images throughout the spheroids. Live cells exhibited green fluorescence, dead cells showed red fluorescence, and the microparticles appeared blue due to their intrinsic reflectance signal. Representative confocal images were collected from multiple spheroids at each time point to evaluate the effect of microparticle treatment on spheroid viability over time.

4.9. SEM imaging of 2D and 3D cultures

Scanning electron microscopy (SEM) was further used to check the uptake of particles at different detectors including Everhart-Thornley Detector (ETD); and Concentric Backscattered Detector (CBS). Cells were grown on round shape cover slips for 2D and in 24-well plates for 3D, treated with different shaped hematite microparticles (100 μg/mL) for 48 h, and were fixed with glutaraldehyde for 30 min at 4 °C. Further, 2D and 3D cultured cells were dehydrated with different ethanol series (30, 50, 70, 100 %). After dehydration, 3D cultured cells were incubated with hexamethyldisilane (HMDS) for 5 min and were drop-casted on glass slides. After drying, coverslips were mounted on stubs and coated with gold with sputter coater for imaging with SEM.

4.10. Confocal analysis for 3D cultured cells

MDA-MB-231 cells and NIH3T3 cells (1×10 [7]) were cultured with 3D matrix in low attachment 6-well plate for 7 days at 37 °C with 5 % CO_2. After 7 days, 3D cultures were treated with different shape microparticles (cubic, ellipsoids, rods) with concentration 100 μg/mL for 48 h. Then, the cultures were washed twice gently with phosphate-buffered saline (PBS) to remove excess microparticles and then fixed with Image-iT™ fixative solutions 3 % glyoxal for 30 min at room temperature, followed by three times PBS wash. Permeabilization was performed using 0.1 % Triton X-100 in PBS for 15 min and followed by blocking with 2 % BSA solution for 30 min. The cells were stained with rhodamine phalloidin diluted (0.5 μL of the 400× stock solution) in PBS and incubated for 20 min at room temperature to visualize the cytoskeletal structure. After washing with PBS, the nuclei were counterstained with DAPI (1 μg/mL) for 10 min. Confocal microscopy was performed on a Nikon AX system using lasers at 561 nm and 405 nm to excite rhodamine and DAPI, respectively. Reflectance imaging of hematite microparticles was carried out using the 647 nm laser line in the green channel with a BS20/80 dichroic mirror to enhance contrast. *Z*-stack images were acquired to generate 3D reconstructions for detailed analysis of microparticle uptake.

4.11. Statistical analysis

Data are presented as mean ± standard deviation from experiments performed in triplicate. Statistical comparisons were conducted using Student's *t*-test in GraphPad software. Differences were considered statistically significant based on calculated *p*-values.

CRediT authorship contribution statement

Navneet Kaur: Writing – review & editing, Writing – original draft, Visualization, Validation, Methodology, Formal analysis, Conceptualization. **Annie Scutte:** Writing – review & editing, Methodology. **Mary Jean Savitsky:** Writing – review & editing, Writing – original draft. **Qi**

Wang: Writing – review & editing, Writing – original draft. **Pitchaimari Gnanasekar:** Writing – review & editing, Formal analysis. **Hannah Matos Pimentel:** Writing – review & editing. **Dazhi Yang:** Writing – review & editing, Supervision. **Jamel Ali:** Writing – review & editing, Supervision, Funding acquisition.

Declaration of competing interest

The authors declare no conflict of interest. The research was conducted in the absence of any commercial or financial relationships that could be interpreted as a potential conflict of interest.

Acknowledgements

This work was funded by the National Science Foundation (EES-2000202, EES-2306449, EES-2219558, and EES-2514451). All the work was performed at the National High Magnetic Field Laboratory, which is supported by National Science Foundation Cooperative Agreement No. DMR-2128556 and the State of Florida. This material is based upon work supported by the National Aeronautics and Space Administration under Award No. 80NSSC24M01745 issued through the Office of STEM Engagement (OSTEM). Mary Jean Savitsky acknowledges support from the Merk Pathways to Successful Biomedical Careers Graduate Fellowship. This material is also based upon work supported by the Air Force Office of Scientific Research under award number W911NF-24-1-0281. The views and conclusions contained in this document are those of the authors and should not be interpreted as representing the official policies, either expressed or implied, of the Air Force Office of Scientific Research or the U.S. Government. The U.S. Government is authorized to reproduce and distribute reprints for Government purposes notwithstanding any copyright notation herein.

Appendix A. Supplementary data

Supplementary data to this article can be found online at https://doi.org/10.1016/j.bioadv.2025.214692.

Data availability

Data will be made available on request.

References

[1] L.G. Griffith, M.A. Swartz, Capturing complex 3D tissue physiology in vitro, Nat Rev Mol Cell Biol. 7 (3) (2006 Mar) 211–224, https://doi.org/10.1038/nrm1858. PMID: 16496023.
[2] L.C. Kimlin, G. Casagrande, V.M. Virador, Mol. Carcinog. 52 (2013) 167.
[3] S. Breslin, L. O'Driscoll, Drug Discov. Today 18 (2013) 240.
[4] J. Lee, M.J. Cuddihy, N.A. Kotov. *https://home.liebertpub.com/teb*.
[5] S.A. Langhans, Front. Pharmacol. (2018) 9, https://doi.org/10.3389/FPHAR.2018.00006.
[6] L.B. Tofani, M.T. Luiz, J.A. Paes Dutra, J.P. Abriata, M. Chorilli, Nanomedicine 18 (2023) 633.
[7] R.L.F. Amaral, M. Miranda, P.D. Marcato, K. Swiech, Front. Physiol. (2017) 8, https://doi.org/10.3389/FPHYS.2017.00605/FULL.
[8] R. Edmondson, J.J. Broglie, A.F. Adcock, L. Yang, Assay Drug Dev. Technol. 12 (2014) 207.
[9] S.G. Anthon, K.P. Valente, Int. J. Mol. Sci. (2022) 23, https://doi.org/10.3390/ijms232314582.
[10] I.T. Swinehart, S.F. Badylak, Dev. Dyn. 245 (2016) 351.
[11] S. Yi, F. Ding, L. Gong, X. Gu, Curr. Stem Cell Res. Ther. 12 (2017) 233.
[12] L.W. Dunne, Z. Huang, W. Meng, X. Fan, N. Zhang, Q. Zhang, Z. An, Biomaterials 35 (2014) 4940.
[13] C. Godugu, A.R. Patel, U. Desai, T. Andey, A. Sams, M. Singh, PLoS One 8 (2013) e53708.
[14] J. Shi, P.W. Kantoff, R. Wooster, O.C. Farokhzad, Nat. Rev. Cancer 17 (2017) 20.
[15] D. Peer, J.M. Karp, S. Hong, O.C. Farokhzad, R. Margalit, R. Langer, Nature Nanotechnology 2 (2007), 12 2007, 2, 751.
[16] N. Kaur, P. Gautam, D. Nanda, A.S. Meena, A. Shanavas, R. Prasad, Bioconjug. Chem. (2024), https://doi.org/10.1021/ACS.BIOCONJCHEM.4C00293.
[17] N. Kaur, P. Sharma, M. Mimansa, R. Jaganathan, A. Munawara, A. Shanavas Aggarwal, Drug Deliv, Transl. Res. 13 (2023) 2520.
[18] A. Tchoryk, V. Taresco, R.H. Argent, M. Ashford, P.R. Gellert, S. Stolnik, A. Grabowska, M.C. Garnett, Bioconjug. Chem. 30 (2019) 1371.
[19] V. Sokolova, J.F. Ebel, S. Kollenda, K. Klein, B. Kruse, C. Veltkamp, C.M. Lange, A. M. Westendorf, M. Epple, Small 18 (2022) 2201167.
[20] S. Sindhwani, A.M. Syed, J. Ngai, B.R. Kingston, L. Maiorino, J. Rothschild, P. MacMillan, Y. Zhang, N.U. Rajesh, T. Hoang, J.L.Y. Wu, S. Wilhelm, A. Zilman, S. Gadde, A. Sulaiman, B. Ouyang, Z. Lin, L. Wang, M. Egeblad, W.C.W. Chan, Nature Materials 19 (2020), 5 2020, 19, 566.
[21] A. Vlachopoulos, G. Karlioti, E. Balla, V. Daniilidis, T. Kalamas, M. Stefanidou, N. D. Bikiaris, E. Christodoulou, I. Koumentakou, E. Karavas, D.N. Bikiaris, Pharmaceutics 14 (2022) 359.
[22] R.Y.P. da Silva, D.L.B. de Menezes, V. da S. Oliveira, A. Converti, Á.A.N. de Lima, Int. J. Mol. Sci. 24 (2023) 5441.
[23] Y. He, K. Park, Mol. Pharm. 13 (2016) 2164.
[24] T.L. Moore, A.B. Cook, E. Bellotti, R. Palomba, P. Manghnani, R. Spanò, S. Brahmachari, M. Di Francesco, A.L. Palange, D. Di Mascolo, P. Decuzzi, Drug Deliv. Transl. Res. 2022 (2019) 12.
[25] A. Lamprecht, U. Schäfer, C.M. Lehr, Pharm. Res. 18 (2001) 788.
[26] J.W. Myerson, A.C. Anselmo, Y. Liu, S. Mitragotri, D.M. Eckmann, V. R. Muzykantov, Adv. Drug Deliv. Rev. 99 (2016) 97.
[27] X. He, Y. Yang, Y. Han, C. Cao, Z. Zhang, L. Li, C. Xiao, H. Guo, L. Wang, L. Han, Z. Qu, N. Liu, S. Han, F. Xu, Proc. Natl. Acad. Sci. USA 120 (2023), https://doi.org/10.1073/pnas.2209260120.
[28] K. Duval, H. Grover, L.H. Han, Y. Mou, A.F. Pegoraro, J. Fredberg, Z. Chen, Physiology 32 (2017) 266.
[29] C. Jubelin, J. Muñoz-Garcia, L. Griscom, D. Cochonneau, E. Ollivier, M. F. Heymann, F.M. Vallette, L. Oliver, D. Heymann, Cell & Bioscience 12 (2022), 1 2022, 12, 1.
[30] R. Edmondson, J.J. Broglie, A.F. Adcock, L. Yang, Assay Drug Dev. Technol. 12 (2014) 207.
[31] X.C. Jiang, A.B. Yu, W.R. Yang, Y. Ding, C.X. Xu, S. Lam, J. Nanopart. Res. 12 (2010) 877.
[32] S. Dasgupta, T. Auth, G. Gompper, Nano Lett. 14 (2014) 687.
[33] "Scanning Electron Microscopy | Electrons in SEM | Thermo Fisher Scientific - US," can be found under https://www.thermofisher.com/us/en/home/materials-science/learning-center/applications/sem-electrons.html, n.d.
[34] J.I. Goldstein, D.E. Newbury, J.R. Michael, N.W.M. Ritchie, J.H.J. Scott, D.C. Joy, Scanning Electron Microscopy and X-ray Microanalysis (2017) 1.
[35] "Reflectance Imaging Using the Nikon A1R Confocal Microscope | News | News & Events | Notre Dame Integrated Imaging Facility | University of Notre Dame," can be found under https://imaging.nd.edu/news-and-events/news/reflectance-imaging-using-the-nikon-a1r-confocal-microscope/, n.d.
[36] E.J. Guggenheim, I. Lynch, J.Z. Rappoport, Int. J. Biochem. Cell Biol. 83 (2017) 65.
[37] S.E.A. Gratton, P.A. Ropp, P.D. Pohlhaus, J.C. Luft, V.J. Madden, M.E. Napier, J. M. DeSimone, Proc. Natl. Acad. Sci. 105 (2008) 11613.
[38] K. Duval, H. Grover, L. H. Han, Y. Mou, A. F. Pegoraro, J. Fredberg, Z. Chen, *doi:*https://doi.org/10.1152/physiol.00036.2016 **2017**, *32*, 266.
[39] P. Cybulski, M. Bravo, J.J.-K. Chen, I. Van Zundert, S. Krzyzowska, F. Taemaitree, H. Uji-i, J. Hofkens, S. Rocha, B. Fortuni, bioRxiv 2024.12.06.626955 (2024).
[40] B.M. Baker, C.S. Chen, J. Cell Sci. 125 (2012) 3015.
[41] J.A. Champion, S. Mitragotri, Proc. Natl. Acad. Sci. USA 103 (2006) 4930.
[42] J.M. Meijer, L. Rossi, Soft Matter 17 (2021) 2354.